



HAL
open science

Experiments support simulations by the NEPTUNE_CFD code in an Upflow Bubbling Fluidized Bed reactor

Florian Sabatier, Renaud Ansart, Zhang Huili, Jan Baeyens, Olivier Simonin

► To cite this version:

Florian Sabatier, Renaud Ansart, Zhang Huili, Jan Baeyens, Olivier Simonin. Experiments support simulations by the NEPTUNE_CFD code in an Upflow Bubbling Fluidized Bed reactor. Chemical Engineering Journal, 2020, 10.1016/j.cej.2019.123568 . hal-02735384

HAL Id: hal-02735384

<https://hal.science/hal-02735384>

Submitted on 2 Jun 2020

HAL is a multi-disciplinary open access archive for the deposit and dissemination of scientific research documents, whether they are published or not. The documents may come from teaching and research institutions in France or abroad, or from public or private research centers.

L'archive ouverte pluridisciplinaire **HAL**, est destinée au dépôt et à la diffusion de documents scientifiques de niveau recherche, publiés ou non, émanant des établissements d'enseignement et de recherche français ou étrangers, des laboratoires publics ou privés.



Open Archive Toulouse Archive Ouverte

OATAO is an open access repository that collects the work of Toulouse researchers and makes it freely available over the web where possible

This is an author's version published in: <http://oatao.univ-toulouse.fr/25248>

Official URL : <https://doi.org/10.1016/j.cej.2019.123568>

To cite this version:

Sabatier, Florian^{ORCID} and Ansart, Renaud^{ORCID} and Huili, Zhang and Baeyens, Jan and Simonin, Olivier^{ORCID} *Experiments support simulations by the NEPTUNE_CFD code in an Upflow Bubbling Fluidized Bed reactor*. Chemical Engineering Journal. ISSN 1385-8947

Any correspondence concerning this service should be sent to the repository administrator: tech-oatao@listes-diff.inp-toulouse.fr

Experiments support simulations by the NEPTUNE_CFD code in an Upflow Bubbling Fluidized Bed reactor

Florian Sabatier^a, Renaud Ansart^{a,*},¹, Huili Zhang^{b,*},², Jan Baeyens^b, Olivier Simonin^c

^aLaboratoire de Génie Chimique, Université de Toulouse, CNRS, INPT, UPS, Toulouse, France

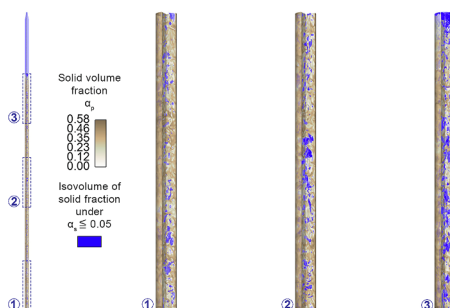
^bSchool of Life Science and Technology, Beijing University of Chemical Technology, Beijing, China

^cInstitut de Mécanique des Fluides de Toulouse (IMFT), Université de Toulouse, CNRS, Toulouse, France

HIGHLIGHTS

- The different fluidization modes in a 4 m long tube are experimentally investigated.
- Fluidization phenomena differ with the tube length (from freely bubbling to slugging).
- Results are used to validate a 3D simulation approach by the NEPTUNE_CFD code.
- The effect of mesh refinement on the slugging behavior prediction is discussed.
- It is demonstrated that experiments and simulation predictions are in good agreement.

GRAPHICAL ABSTRACT



ABSTRACT

Long tubes with small internal diameter find increasing applications in indirect concentrated solar receivers using an Upflow Bubbling Fluidized Bed of Geldart-A powders as heat carrier. Although successfully demonstrated for tubes of 0.5 to 1 m length, longer tubes are required to increase the solar energy capture efficiency and capacity. The fluidization phenomena differ with the tube length, and freely bubbling fluidization will be transformed into slugging, thus hampering the heat transfer. The behavior of Geldart-A powders in tall tubes of small I.D. has not been extensively studied. The research experimentally investigated the different fluidization modes in a 4 m long tube, and demonstrated the occurrence of freely bubbling at the bottom section of the bed, and slugging from a bed depth in excess of about 1.25 m. Slug characteristics (frequency, length, velocity) were measured and correlated. The results were used to validate 3D numerical simulations based on an Euler-Euler approach in the NEPTUNE_CFD code applied to a fine mesh of 15,000,000 cells. A positive match between experimental and simulation results concerning frequency and velocity of large bubble structures was obtained. The effect of mesh refinement on the slugging behavior prediction was discussed.

* Corresponding authors.

E-mail addresses: renaud.ansart@ensiacet.fr (R. Ansart), zhhl@mail.buct.edu.cn (H. Zhang).

¹ Numerical simulation.

² Experiments.

Nomenclature

Roman symbols

C_d	drag coefficient (-)
D	column diameter (m)
d_{50}	powder distribution median volume diameter (m or μm)
d_B	bubble diameter (m)
d_{drag}	drag diameter (m or μm)
$d_{[m;n]}$	powder distribution specific [m;n] diameter according to
	$d_{[m;n]} = \left(\frac{\int_{d_{min}}^{d_{max}} d^{mf}(r) dr}{\int_{d_{min}}^{d_{max}} d^{nf}(r) dr} \right)^{\frac{1}{m-n}} \quad (\text{m or } \mu\text{m})$
d_p	particle diameter (m or μm)
d_{sv}	powder surface/volume diameter (m or μm)
e_c	particle-particle normal restitution coefficient (-)
e_w	particle-to-wall restitution coefficient (-)
f_s	slug frequency (Hz)
g	gravitational constant (m s^{-2})
H	expanded bed height (m)
H_{mb}	expanded bed height at $U = U_{mb}$ (m)
H_{mf}	expanded bed height at $U = U_{mf}$ (m)
k_N	Newton regime non-sphericity drag correction coefficient (-)
k_S	Stokes regime non-sphericity drag correction coefficient (-)
L	distance between distributor level and measurement level along the bed height (cm)
L_S	slug length (cm)
q_p^2	mean particle random kinetic energy (m^2s^{-2})
Re_p	particle Reynolds number (-)
U	fluidization velocity (m s^{-1})
$U_{k,i}$	mean velocity of phase k (m s^{-1})

U_{mb}	minimum bubbling velocity (m s^{-1})
U_{mf}	minimum fluidization velocity (m s^{-1})
U_S	slug velocity (m s^{-1})
U_t	terminal settling velocity (m s^{-1})
W_S	slug interval (cm)
x, y, z	cartesian coordinates in the tube: x, y in the cross section, z oriented opposite to the gravitational force (m)
r, θ	polar coordinates projected in plan view x/y , (m and rad respectively)

Greek symbols

α_k	volume fraction of phase k (-)
$\alpha_{s,min}$	frictional viscosity activation threshold (-)
$\alpha_{s,max}$	maximal particles compaction (-)
ΔP	Average pressure drop across the fluidized (Pa)
$\delta(\Delta P)$	fluctuations of the pressure drop (Pa)
Δ_r	Radial cell size (m)
Δ_z	Axial cell size (m)
Δ_l	2D grid cell size (m)
ε_B	bubble fraction (-)
ε	bed voidage (-)
μ_g	gas viscosity (Pa s^{-1})
ϕ	average particle sphericity (-)
ρ_k	density of phase k (kg m^{-3})
ρ_B	Bulk density (kg m^{-3})

Subscripts

g	gas
s	solid

1. Introduction

Gas/solid fluidization powders can involve C (cohesive), A (aeratable), B (bubbling) and D (coarse) particles [1–3]. The different powder groups can be expressed in terms of the relevant particle size, d_p , and gas/solid densities, ρ_g and ρ_s [1,4].

For cristobalite sand, used in the present research ($\rho_s \sim 2640 \text{ kg m}^{-3}$), C powders will be smaller than $33 \mu\text{m}$; the aeratable group A will cover the range of 33 to $86 \mu\text{m}$; group B powders will range from 86 to $446 \mu\text{m}$; and group D powders will have a particle size in excess of $446 \mu\text{m}$. Although aeratable group A powders are widely used in commercial fluidized bed catalytic reactors [5], their recent application in Upflow Bubbling Fluidized Bed (UBFB) or Cross-flow Bubbling Fluidized Bed (CfBFB) indirect solar receivers opens new application perspectives [6–11] due to their high mobility [12], high wall-to-bed heat transfer rates [13], and their easy circulation around the concentrated solar energy loops. Gas bubbles in group A powders moreover split and recombine frequently, resulting in a maximum stable bubble size [1,14], as further discussed in the paper. The bubble size is independent of the average particle size in Geldart-A powders. The bubble rise velocities appear to be ~ 0.3 to 0.4 m s^{-1} , irrespective of the bubble size, suggesting that the gross powder circulation controls the rise velocity [1,14,15]. Bubbles will transform into slugs at sufficiently high superficial gas velocity or in deep beds, as illustrated in Fig. 1. Slugs reduce particle mixing and minimize the gas/solid contacting [13] and reduce the wall-to-bed heat transfer coefficient [12]. Bubbling and slugging are distinct hydrodynamic modes in a fluidized bed and should therefore be jointly considered in predicting chemical conversions and heat transfer. At velocities in excess of 0.5 m/s , depending on the particle size, a turbulent or ultimately circulating fluidized bed mode will occur and particle recycling is required to maintain the bed solids' inventory

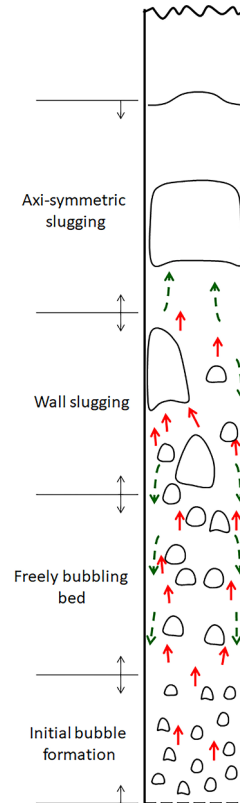


Fig. 1. Bubbling and slugging modes.

[16–18]. Small Internal Diameter (I.D.) beds are normally used in laboratory scale experiments, or represent the constrained bed cells in between vertical heat exchanger tubes in a catalytic reactor [5]. The current development of particle suspension solar heat receivers use such small I.D. beds with Geldart-A powders as heat carriers [8,9]. Fig. 2 depicts the layout of a 3 MW_{th} hybrid combined cycle solar tower power plant, to be tested on pilot-scale at the CNRS-Themis solar tower (France), without the steam block [6,7,9]. The pilot-scale set-up is described elsewhere and includes the particle suspension receiver, hot particle storage [19], and crossflow fluidized bed air heater to preheat the turbine compressed air [6,7]. Exhausts from the turbine are fed to a steam block. The design of the receiver is of paramount importance in order to be able to operate at as high a temperature as possible (750 to 850 °C).

The present work considers the scale-up of the Upflow Bubbling Fluidized Bed (UBFB) receiver concept. Previous papers have provided information concerning the on-sun testing of a single tube (36 mm I.D., 0.5 m long) and of a 150 kW_{th} pilot module consisting of 16 parallel tubes of 29.7 mm I.D., each 1 m long, using group A powders fluidized at superficial gas velocities of ~0.03 to 0.20 m s⁻¹ [9,11,20,21]. A further scale-up to multi-MW capacity will involve the use of the parallel tube-concept with larger I.D. tubes and of taller height towards an optimum use of the concentrated heliostat beams and provide sufficient heat capture surface area. Although receiver heights of 10 to 18 m are now common practice in molten salt applications [22], the gas-solid hydrodynamics in the UBFB will limit the maximum applicable height in function of the tube geometry, with special emphasis on its height, due to the occurrence of slugging (Fig. 1). The onset of slugging mostly depends upon the tube diameter and the excess gas velocity, i.e. $U - U_{mf}$ [1]. Since slugs have a limited bubble-induced particle mixing, they reduce the wall-to-bed heat transfer [13]. It is hence important to investigate the bubbling/slugging effects in a geometry similar to the currently scaled-up particle-in-tube concept.

The novelties of the present paper and the objectives are hence clearly defined, and result from the use of extensive experimental data in support of a dedicated NEPTUNE_CFD code simulation. The objectives involve a stepwise approach that:

- (i) fully assesses properties of the system under scrutiny, with special emphasis on secondary particle properties such as size distribution and sphericity;
- (ii) studies the hydrodynamic behavior of selected particles experimentally in a small I.D. tube of 4 m height;
- (iii) introduces relevant simulation conditions into the NEPTUNE_CFD code, to define simulation geometry and mesh, fix boundary conditions (inlet, outlet, tube walls), and assesses the influence of the relevant particle and air properties;
- (iv) applies an Euler-Euler model, with governing equations described by Ansart et al. [23];
- (v) validates the approach through pressure gradients and solid volume fraction;
- (vi) compares experimental and simulation results towards slug formation, slug frequency, velocity, and occupancy profiles along the tube diameter and height;
- (vii) discusses the effect of refining the mesh characteristics on the slugging behavior prediction for Geldart-A powders;
- (viii) formulates fluid-dynamic conclusions and recommendations.

2. Experimental setup and procedures

2.1. Equipment and powders used

Within the concept of a “particle-in-tube” UBFB, a small I.D. cylindrical column was used of 50 mm I.D. and of a total height of 4 m, hence complementing the experimental research of Kong et al. [1], limited to a 2 m high tube. Experimental procedures were detailed by Kong et al. [1] and involve an operating air flow rate in the range of 0 to 5×10^{-4} kg s⁻¹. The fluidized bed is fed by compressed air at ambient temperature and the bed exhaust is connected to atmosphere. The distributor plate had a pressure drop of 1560 Pa at a superficial air velocity of 0.1 m s⁻¹, significantly exceeding the common design recommendations [24]. The Geldart-A powder used was cristobalite silica. Particle properties were defined by the methods described by Kong et al. [1], with mean particle size of 55 μm, absolute density of 2640 kg m⁻³ and tapped bulk density [3] of 1380 kg m⁻³. U_{mf} was

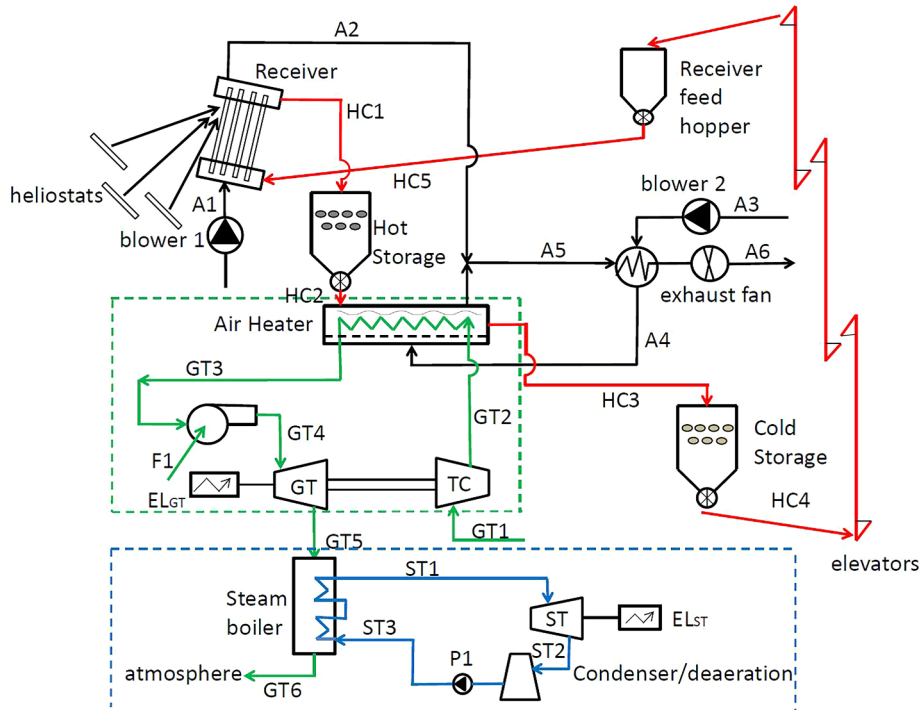


Fig. 2. Schematics of a solar tower combined cycle generation process [7].

determined from a common ΔP versus U graph, and was 0.34 cm s^{-1} . The minimum bubbling velocity of 0.53 cm s^{-1} corresponded with the superficial air velocity when first bubbles could be seen erupting at the bed surface. The accuracy on U_{mf} was 0.01 cm s^{-1} while being 0.02 cm s^{-1} for U_{mb} . Values of U_{mf} and U_{mb} are clearly different. The particle shape was determined by OPTEC DV 320 microscope imaging and the sphericity (ϕ) varying between 0.64 and 0.71 was calculated from Cavarretta et al. [25] and Cho et al. [26]. U_t was calculated as 0.203 m s^{-1} according to the method described by Geldart [3]. For the minimum fluidization height of 230 cm, the column was filled with 5 kg of solid.

2.2. Measuring techniques

The behavior of fluidized beds at the onset of slugging and full slugging mode was assessed by three different methods, as previously used by Baeyens and Geldart [2] and Kong et al. [1]. Visual observations, pressure drop and its fluctuations and high speed camera imaging were jointly used and assessed. Whereas visual observations cannot be used in the bottom (bubbling) section of the bed due to overlapping bubbles, and pressure drop measurements show significant fluctuations, the combined analyses of the three methods provided a satisfactory insight into the full slugging mode. Photographic illustration of the observed wall and axi-symmetric slugs is given in Fig. 3.

2.3. Experimental procedure

The bed heights at U_{mf} and U_{mb} were measured. The gas velocity was then increased to well into the slugging regime. Flow rate readings, visual and ΔP observations, and images were made for given periods of time (between 2 and 3 min). All data points presented in the figures are averages of 3 repeat experiments. The deviation among 3 repeat results and the averages was below 5%. The evolution of expanded bed height (H) in relationship with the bed height at minimum bubbling (H_{mb}) with excess gas velocity is illustrated in Fig. 4. The time average pressure drop across the whole bed ΔP , and the pressure fluctuations, presented as standard deviation to the average pressure drop $\delta(\Delta P)$, were recorded and presented as ratio in Fig. 5. Leva et al. [27] tentatively predicted the onset of slugging when pressure fluctuations exceed 5 per cent of the pressure drop through the bed at the given gas flow rate. This rule of thumb was in fair agreement with our observations.

At $(U - U_{mf})$ values beyond the onset of slugging, big bubbles rapidly transformed into wall-slugs, which prevailed throughout the bed height for about 1.25 m. They are subsequently transformed into axi-

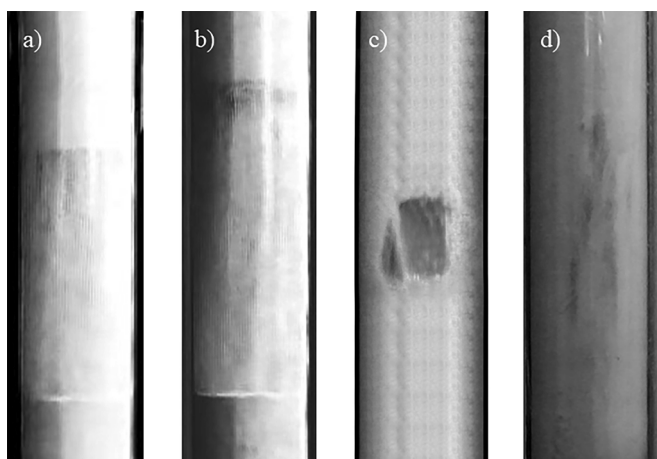


Fig. 3. Photographic illustrations of Axi-symmetric slugs in the powder at the level of 150 cm in the bed: a) $U - U_{mf} = 9 \text{ cm s}^{-1}$ b) $U - U_{mf} = 12 \text{ cm s}^{-1}$, and wall slugs in the powder at the bed level of 90 cm: c) $U - U_{mf} = 9 \text{ cm s}^{-1}$; d) $U - U_{mf} = 12 \text{ cm s}^{-1}$.

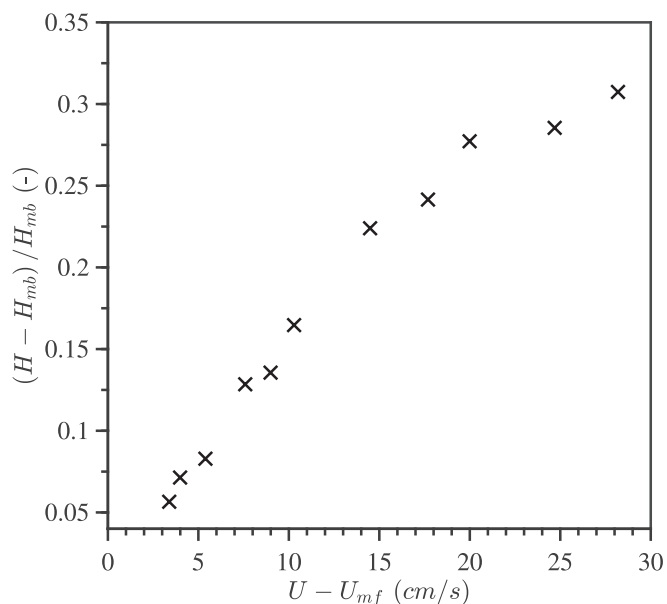


Fig. 4. Total bed height fluctuations with $U - U_{mf}$ for the cristobalite powder at $H_{mf} = 230 \text{ cm}$, and $H_{mb} = \sim 270 \text{ cm}$.

symmetric slugs in deeper beds. The axi-symmetric slugging mode hampers the heat transfer from the receiver wall to the bed (poor solids mixing and long contact of an air slug with the wall). Further experimental results will be given in Section 4 below.

3. Numerical simulation description

3.1. Mathematical model

3.1.1. Eulerian modeling approach

To access to the particle behavior inside the receiver tubes, two CFD approaches (Eulerian-Lagrangian or Eulerian-Eulerian) can be used. The Eulerian-Lagrangian approach treats particles as discrete elements when the fluid flow is characterized by Eulerian equations. The motion for each individual particle is solved, with inclusion of the effects of

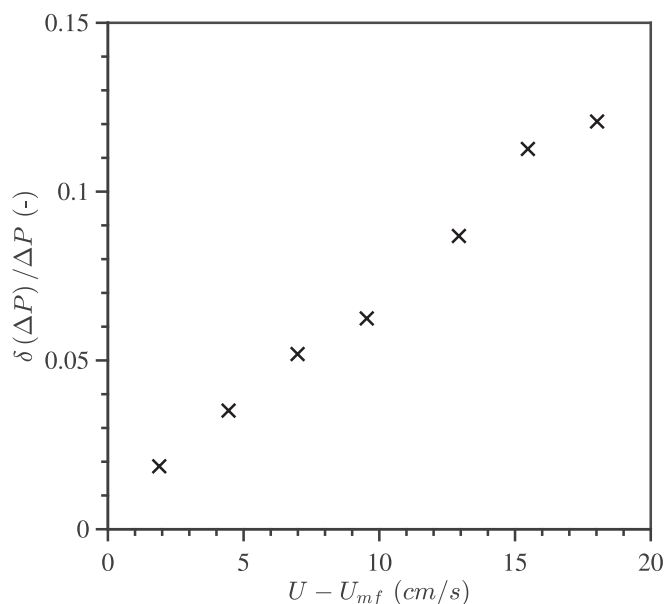


Fig. 5. Relative standard deviation of pressure ($\delta(\Delta P) / \Delta P$) versus $U - U_{mf}$ for cristobalite powder, measured across the total bed height, for $H_{mf} = 230 \text{ cm}$.

particle collisions and forces acting on the particles due to the gas [28]. For this method to be very accurate, every particle has to be taken into account, likewise every particle-particle and particle-wall collisions. Since the calculation time is directly linked to the number of particles simulated, in the specific case studied here, with a particle size less than 100 μm , more than 10^{11} particles need to be accounted for. This approach is clearly impossible to solve with current calculation resources. The Eulerian-Eulerian approach treats particle and fluid phases as interpenetrating yet separated and continua; although coupled Eulerian transport equations for mass, momentum, and energy are written for both phases. This modeling approach allows the simulation of large fluid-particle systems, including reactive flow, heat transfers [29,30] and polydisperse systems [31,32]. In this approach, particles size and inertia are linked to the mesh size: with very small and light particles, calculation time may still be a difficulty to overcome.

Three-dimensional numerical simulations of the fluidized bed were performed using the NEPTUNE_CFD code. This Eulerian n-fluid unstructured parallelized multiphase flow software [33] is developed in the framework of the NEPTUNE project, rallying CEA (Commissariat à l'Énergie Atomique), EDF, IRSN (Institut de Radioprotection et de Sûreté Nucléaire), and Framatome. The modeling approach for turbulent polydisperse gas-solid flows is implemented by the Institut de Mécanique des Fluides de Toulouse (IMFT) and the Laboratoire de Génie Chimique (LGC) and has been developed for High Performance Computing [29].

3.1.2. Mathematical models implemented

The mathematical approach used is a hybrid method [34] deriving transport equations by phase ensemble average for the fluid phase and including the effects of the interstitial fluid towards the dispersed phase by the kinetic theory of granular flows [35]. The frictional stress tensor is taken into account in the particle stress tensor using the model proposed by Srivastava and Sundaresan [36], with a threshold value for the frictional viscosity activation $\alpha_{s,min} = 0.55$ and a maximal particles compaction of $\alpha_{s,max} = 0.64$. Transport equations (mass, momentum and fluctuating kinetic energy) are solved for each phase and coupled through interphase transfer terms. The drag law used is based on two different correlations (Wen and Yu [37] and Ergun [38]) depending on the value of the solid volume fraction [39,40]. The gas flow is considered as laminar because the variance effects of gas local velocity in the equation of momentum are negligible likened it to the drag term. Finally, q_p^2 , the particle random kinetic energy, is integrated in a transport equation through the solid phase. All mathematical equations are described by Ansart et al. [23].

3.1.3. Consideration of powder PSD and non-sphericity

As shown in Figs. 6 and 7, the powder used presents a very broad particle size distribution. Since particles follow a Gaussian-like monomodal size distribution, the complete size distribution was simplified to a single particle class with two separate diameters: (See Fig. 8)

$$d_{drag} = \sqrt{\frac{d_{[3,0]}^3}{d_{[1,0]}}} \quad (1)$$

d_{drag} for the drag coefficient term, as defined in Eq. 1 and $d_p = d_{50}$, the median diameter, for every other equation (momentum transfer, random kinetic energy, collisions) as previously applied by Sabatier et al. [41]. The drag term coefficient of Gobin et al. [39] was modified to include effects of non-sphericity based on the work of Bagheri and Bonadonna [42] as expressed in Eqs. (2). Two coefficients k_N and k_S were introduced, correcting the drag term in the Stokes and Newton regime respectively, and determined by the measurement of two shape factors defined by Bagheri and Bonadonna [42].

$$C_d(Re_p) = \begin{cases} C_{d,WYnsp} & \text{if } \alpha_g \geq 0.7 \\ \min[C_{d,WYnsp}, C_{d,Ergnsp}] & \text{else } \alpha_g < 0.7 \end{cases} \quad (2.a)$$

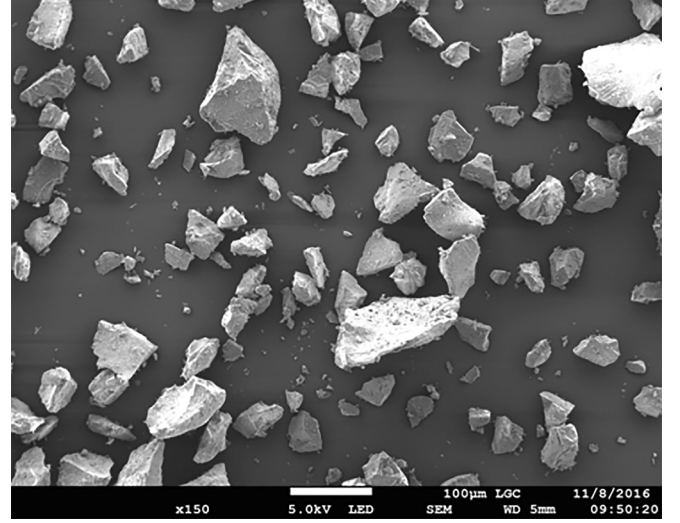


Fig. 6. SEM photograph of powder at 150 \times magnification.

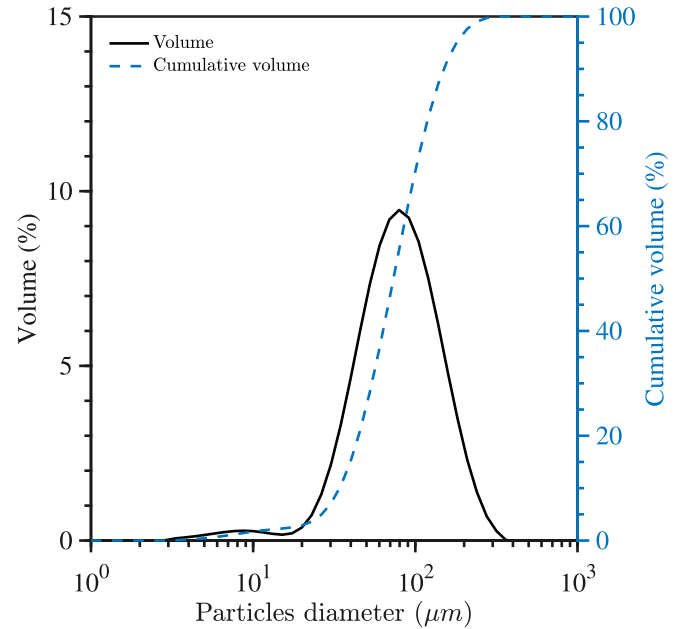


Fig. 7. Cristobalite powder PSD, analysis by Malvern MS2000.

$$C_{d,WYnsp} = \frac{24k_S}{Re_p} \left(1 + 0.125 \left(Re_p \frac{k_N}{k_S} \right)^{2/3} + 0.46 \frac{k_N}{1 + \frac{5300}{Re_p k_N / k_S}} \right) \alpha_g^{-1.7} \quad (2.b)$$

$$C_{d,Erg} = 200k_S \frac{(1 - \alpha_g)}{Re_p} + \frac{7}{3} k_N, \quad Re_p = \alpha_g \frac{\rho_g |\vec{v}_r|_p d_p}{\mu_g} \quad (2.c)$$

$$V_{p,i} = \langle v_{r,i} \rangle_p = U_{p,i} - U_{g,i} \quad (2.d)$$

3.2. Geometry and mesh

3.2.1. Geometric model

The geometric model used for simulation was the experimental 4 m long pipe of 5 cm I.D., followed by a convergent head. To prevent the occurrence of a local exit pressure drop that could result in a numerical error for the code, the convergent head (although not used experimentally) accelerates the particle suspension before the tube exhaust, in order to prevent occasional backflow and thus numerical artifacts.

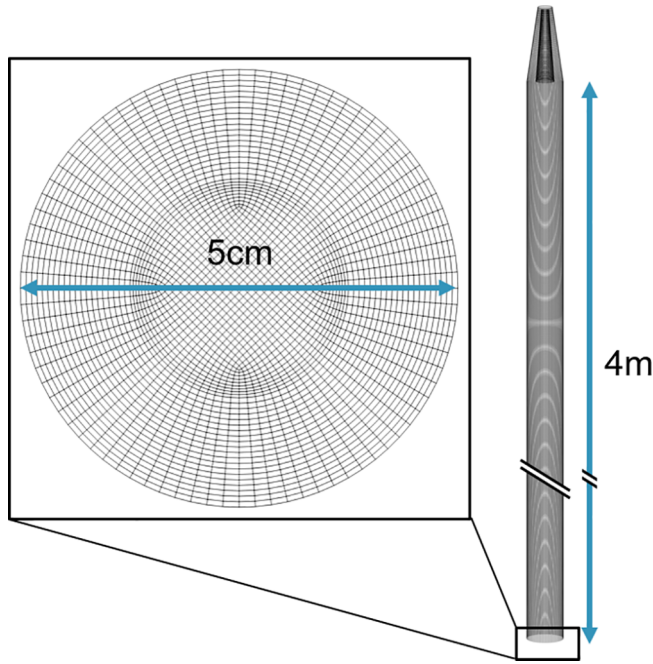


Fig. 8. 3D mesh for the numerical simulation 15,000,000 cells.

Geldart-A particles are highly sensitive to the mesh cells size, but a mesh-independent solution based on the bed expansion is possible [43,44]. A sensitivity study was performed on columns of the same diameter but only of 1 m height. This study was based on the convergence of the spatially averaged solid fraction α_s , depending on the mesh nodes number on a diameter. For each case, $\Delta r = (\text{nodes on a diameter} - 1)/D$ and $\Delta z = \sqrt{2} \Delta r$. Table 1 shows the evolution of the solid volume fraction α_s , spatially averaged over the bed. As the mesh cells size decreases, the spatially averaged solid volume fraction increases, thus reflecting a bed height decrease. Beyond 80 nodes along the bed diameter, the average solid volume fraction is almost constant (less than 1% variation). Due to computational resources, the rest of the study will hence focus on a 80 nodes along the bed diameter mesh. Finally the mesh used for the simulation is built from about 15,000,000 hexahedrons of approximately $\Delta r = 0.63$ mm and $\Delta z = 0.89$ mm.

3.2.2. Phase properties

The particles used for the simulation were cristobalite silica, fluidized by air at atmospheric pressure (101325 Pa) and ambient

Table 1

Instantaneous solid volume fraction α_s at $t = 60$ s, spatially averaged within a vertical slice from $z = 0$ to $z = 50$ cm.

nodes number on the tube diameter	60	70	80	90
spatially averaged solid fraction α_s	0.282	0.288	0.295	0.297

Table 2

Phases properties used for the numerical simulation (air and powder).

Gas density at $P = 101.3$ kPa and $T = 298$ K	Gas dynamic viscosity	Absolute particle density	Particle median volume diameter, d_{50}	Drag diameter, d_{drag}	k_S	k_N	Particle-particle restitution coefficient, e_c	Frictional viscosity activation threshold, $\alpha_{s,min}$	Maximal particles compaction, $\alpha_{s,max}$
kg m^{-3}	Pa s	kg m^{-3}	μm	μm					
1.1847	1.85×10^{-5}	2640	73.3	45	1.5	4	0.9	0.55	0.64

temperature (298 K). Due to the bed height, the pressure gradient along the tube height cannot be neglected and the gas density cannot be considered as constant but needed to be computed using the perfect gas law. It is noteworthy that cinematic viscosity is automatically computed by the code from density and dynamic viscosity. The initial solid mass in the column for numerical simulations was 5 kg. Phase physical properties used for the simulation are summarized in Table 2.

3.2.3. Boundary conditions

Due to the mesh size, numerical simulations were highly CPU-time consuming and therefore only one intermediary velocity case was studied. The industrial gas velocity operating range for the UBFB in solar receivers ranges from 7 to $56 \times U_{mf}$, with an average fluidization velocity of $25 \times U_{mf}$. The distributor was considered as a horizontal wall for the particles and an inlet with an imposed uniform superficial velocity for the gas, equals to $U = 25 \times U_{mf} = 0.085 \text{ m s}^{-1}$. Due to the expansion of the gas flow towards the top of the bed, the superficial gas velocity will increase and close to $30 \times U_{mf} = 0.102 \text{ m s}^{-1}$. At the top of the fluidized bed, a free outlet for both gas and particles was defined. The same wall-type boundary condition was applied for both the particles at the distributor, and for both phases at the side walls: this condition involves no-slip for velocity, and zero-flux for random kinetic energy for the solid phase, corresponding to a large wall roughness or a high non-sphericity of the particles [45]. It is noteworthy that no-slip boundary condition was assumed over partial-slip boundary condition due to the lack of tube roughness measurement and thus the impossibility to accurately justify for a value of the models friction and bouncing parameters. In addition, the no-slip boundary condition, considering elastic frictionless bouncing at the walls, and thus with a particle-to-wall restitution coefficient $e_w = 1$, was found to be in good agreement with PEPT experimental measurements for dense fluidized beds [45].

3.2.4. Simulation procedure

Numerical simulations have been carried out on 700 parallelized cores. Classically, to post-treat and analyze results from instantaneous numerical simulation, calculations on long physical times (> 100 s) are needed in order to extract converged temporal averages of simulated physical quantities. But for this simulation, jointly due to the very high fluctuation induced by the crossing of slugs, the tube height and the slug velocity, physical times of more than 500 s would be needed to achieve converged statistic time average, which would represent months of calculation. Consequently, new post-treatments were developed, focusing on their convergence speed. Every calculation hence followed a three-step scheme, where the first 20 seconds account for a transitory regime, including the initial bed destabilization; a 30 seconds of hydrodynamic transition to complete fluidization; and finally, a 50 seconds calculation allows to extract instantaneous variables for each mesh cell at a 20 Hz frequency. This time delay is certainly sufficient, since the axi-symmetric slug velocity is around 0.4 m s^{-1} and with a frequency of ~ 0.5 to 1 Hz according to Kong et al. [1]. The time step was adaptive and calculated in order to respect a Courant-Friedrich-Levy and a Fourier condition inferior to 1 and 10 respectively. The convergence criterion was calculated through the sum of every volume

fraction according to $\max_{i \in ncel} (1 - \sum_k \alpha_s(i)) < \varepsilon_{vol}$, where i is a given cell within the whole domain $ncel$ and ε_{vol} is set to 10^{-8} . The partial differential equations are discretized with a second-order centered scheme and the solution is time-advanced by a first order scheme. The numerical methods used by NEPTUNE_CFD are further described by Hamidouche et al. [29] and Neau et al. [46].

4. Results and discussion

4.1. Experimental results

4.1.1. Slug description

The slug frequency, as determined by high speed camera, varies with the considered level in a bed of given total height, as illustrated in Fig. 9 using the average values obtained by imaging and pressure drop measurements. Combining earlier literature findings [47–49], Kong et al. [1] proposed equations for the slug frequency, f_s , the slug length, L_s , and the slug intervals, W_s . Essential equations are repeated hereafter.

$$f_s = \frac{U - U_{mf}}{L_s} \quad (3)$$

$$L_s = \frac{(U - U_{mf})kD^{1/2}}{(0.35 \text{ or } 0.7)g^{1/2}} \quad (4)$$

Substituting (4) in (3) assuming $W_s = kD$, and $U_s = 0.35(gD)^{1/2}$ for axi-symmetric, or $U_s = 0.7(gD)^{1/2}$ for wall slugs [1] gives

$$f_s = \frac{(0.35 \text{ or } 0.7)g^{1/2}}{kD^{1/2}} \quad (5)$$

The slug frequency is independent of the gas velocity, as confirmed by the experiments, and the constant k must be experimentally determined. Average slug frequencies were determined and were illustrated in Fig. 9.

Frequencies level off for bed levels exceeding 100 to 150 cm, and axi-symmetric slugs start to form at heights exceeding approximately 150 cm. For bed levels above ~ 1 m, when wall slugs are completely formed, f_s is independent of L and about 1 Hz. The data obtained are

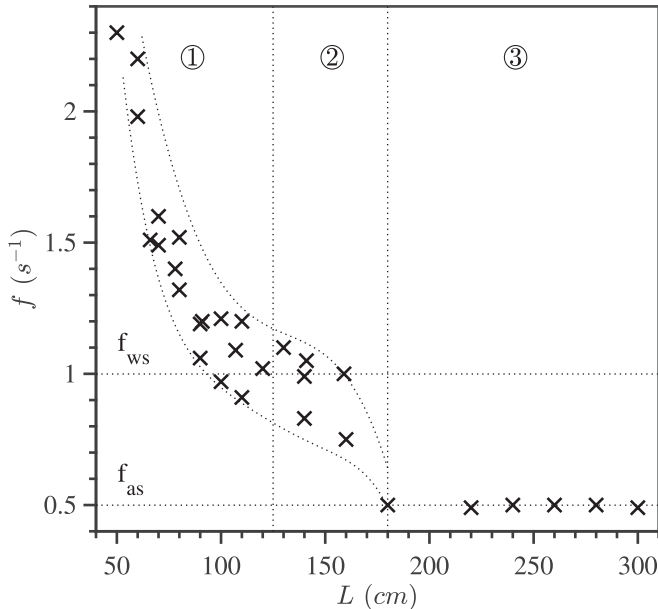


Fig. 9. Bubble and/or slug frequency, f (s^{-1}) versus level of measurement in the bed at $U - U_{mf} = 12.7 \text{ cm s}^{-1}$. Regimes: ① freely bubbling, ② wall slugging and transition to axi-symmetric slugging, ③ axi-symmetric slugging; f_{ws} and f_{as} : expected frequency limits for wall slugging and for axi-symmetric slugging, respectively.

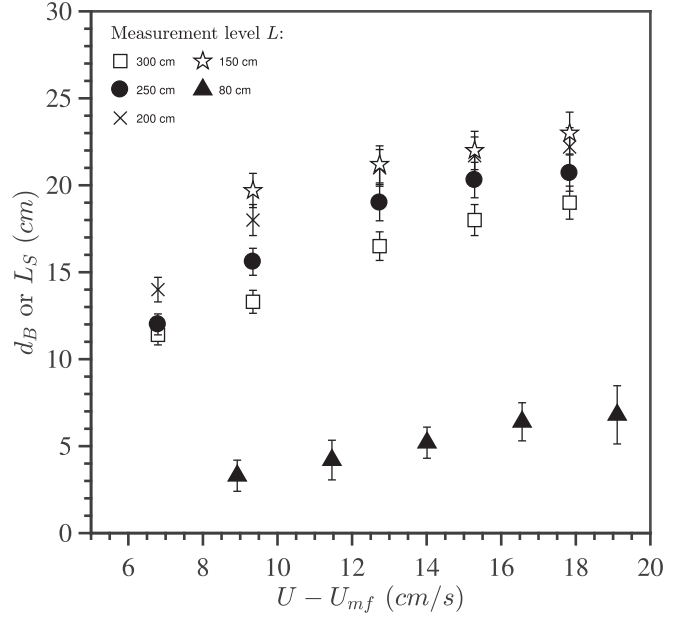


Fig. 10. Illustration of bubble diameters or slug lengths at different excess gas velocities for cristobalite, measured at different bed levels in a bed of $H_{mf} = 300 \text{ cm}$.

$\sim 30\%$ higher than proposed earlier by Baeyens and Geldart [2]. For axi-symmetric slugs, the equilibrium slug frequency is 0.5 Hz. The slug length is a nearly linear function of $U - U_{mf}$, as illustrated for the experimental measurements in Fig. 10, and corresponds with the prediction of Eq. (4). Wall slug lengths of 2 to $\sim 15 \text{ cm}$ were imaged at specific levels in the bed and for a given excess air flow rate. Axi-symmetric slugs with length of over 15 cm were imaged at bed levels in excess of 1.5 m and higher values of $U - U_{mf}$.

The level in the bed clearly determines the slug length at a given $U - U_{mf}$, and slug growth continues along the level in the bed by further coalescence. From the image analysis, the slug velocity was also determined and plotted in Fig. 11.

The bubble or slug velocities increase slightly with excess gas velocity, irrespective of the level in the bed when exceeding 0.8 m. The measured slug velocities correspond with the theoretical prediction of the wall-slugging regime, as indicated in the Figure caption. At lower levels in the bed, wall slugs transform into axi-symmetric slugs with velocities according to the appropriate equation, at higher $U - U_{mf}$ values.

When the level in the bed exceeds 1.5 m, slug velocities dropped to ~ 0.3 to 0.4 m s^{-1} , corresponding to axi-symmetric slugs, as calculated from:

$$U_s = (U - U_{mf}) + 0.35\sqrt{gD} \quad (6)$$

4.1.2. Solids fraction

The bubble fraction ε_B , the bed voidage ε and the solids fraction $\alpha_p = (1 - \varepsilon)$ were calculated from the experimental results and are presented in Figs. 12 and 13, respectively. The bubble fraction was calculated from the bed expansion data ($\varepsilon_B = 1 - H_{mf}/H$). The bed solids fraction was determined from the measured pressure drop across the bed ($\Delta P = [\rho_s(1 - \varepsilon)gH]$). The bubble fraction in the bed is considerably higher than that for group B powders (expected < 0.1), and the expanded bed is characterized by a fairly low solids fraction [1,12]. Both values are important in calculations of e.g. the heat transfer coefficient where a surface renewal model strongly depends upon both α_p and ε_B . Heat transfer measurements and its modeling are the subject of ongoing research.

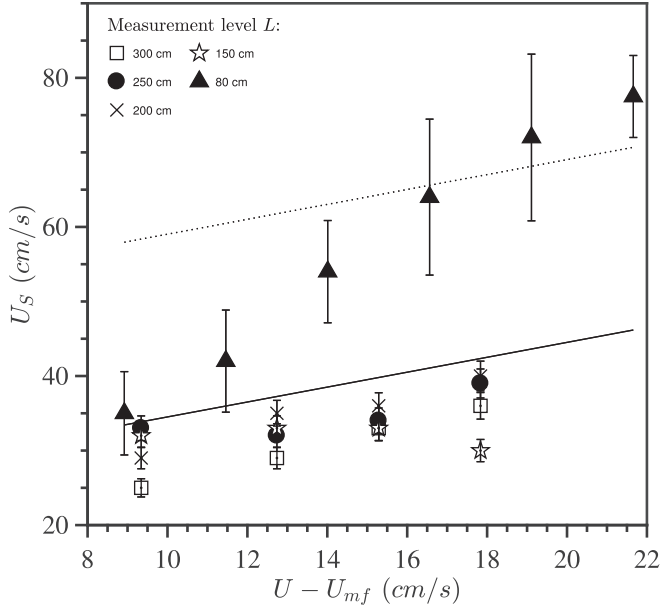


Fig. 11. Slug velocity versus $U - U_{mf}$, measured at different bed levels in a bed of $H_{mf} = 300$ cm. — $U_{ws} = (U - U_{mf}) + 0.7\sqrt{gD}$ and $U_{as} = (U - U_{mf}) + 0.35\sqrt{gD}$.

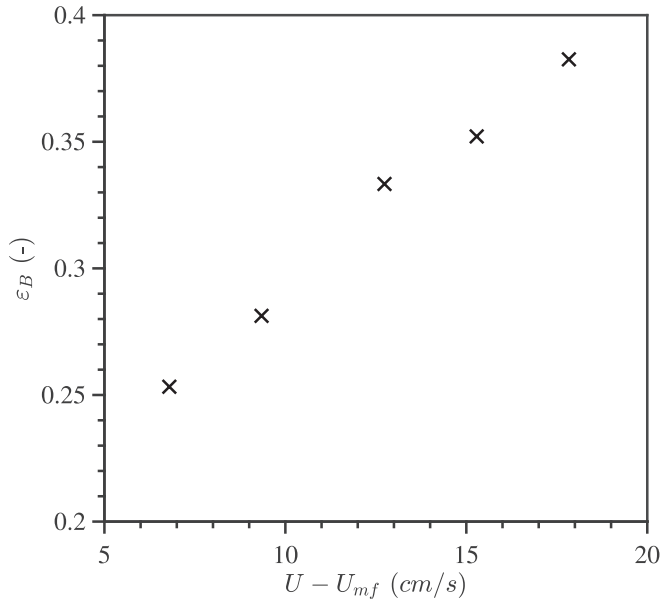


Fig. 12. Illustration of the average bubble fraction ϵ_B versus $U - U_{mf}$ in a bed of $H_{mf} = 300$ cm.

4.2. Comparison with simulation results

4.2.1. Pressure gradient along the bed height

In order to validate the simulation results, the pressure drop across the bed was compared with the experimental results at $U - U_{mf} \approx 0.099 \text{ m s}^{-1}$. It was found to average to solid fraction of $\alpha_s = 0.29$, in fair agreement with experimental results of Fig. 13 ($\alpha_s \approx 0.33$), considering the inaccuracy of measuring ΔP across the bed when considerable fluctuations occur due to slugging. The slug frequency is shown to be independent of the excess air velocity. Since the volumetric excess gas flow rate equals the product of slug frequency and slug volume, the slug length for a constant frequency and slug diameter (\sim tube diameter), will slightly increase from the onset height to the top of the bed: the hydrostatic pressure indeed decreases with bed height, and the

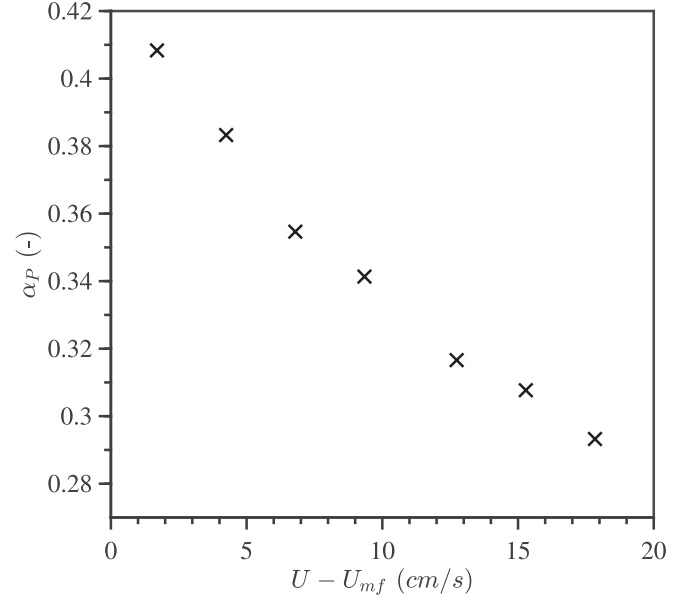


Fig. 13. Calculated average solids fraction, $\alpha_p = (1 - \epsilon)$ in a bed of $H_{mf} = 300$ cm.

air expands from 1.47 kg m^{-3} at the bottom of the bed to 1.18 kg m^{-3} at the top. The air superficial velocity hence increases from $25 \times U_{mf}$ at the distributor to $30 \times U_{mf}$ at the top of the bed, meaning that the slug length will increase by maximum 20% towards the top of the bed.

4.2.2. Bed height fluctuations $\delta(\Delta P)/\Delta P$

In the same way as for experiments, the pressure fluctuations were monitored just above the distributor and the ratio of pressure fluctuation to total pressure drop was determined. This ratio was predicted to be 0.06 against the experimentally measured 0.065 at $U - U_{mf} \approx 0.099 \text{ m s}^{-1}$ (Fig. 5). Pressure fluctuations above 5% meet the criterion of Leva et al. [27] for the onset of slugging.

4.2.3. Spatially averaged instantaneous solid volume fraction along the bed, $\alpha_s(z, t)$

As explained before, new post-treatments had to be developed to avoid convergence issues as found with standard physical quantities' horizontal profiles. Thus, the instantaneous solid volume fraction $\alpha_s(r, \theta, z, t)$ was spatially averaged over cylindrical slices defined along the vertical z axis, with their diameter equal to the tube I.D. and with a vertical span of about 9.55 mm. Fig. 14 illustrates the evolution of this spatially averaged solid fraction $\alpha_s(z, t)$ along the tube height, at a given time $t = 71.9$ s. Similar results have been obtained for several time steps but for clarity only this single simulation time is presented. From the bottom to the top of the tube, two patterns are distinguishable, an initial unstructured small fluctuation corresponding to bubbling flow, followed by stronger isolated peaks highlighting the presence of large bubbles or slugs. In order to filter out bubbling flow, a threshold value, based on a simplified bubble-emulsion model and $d_B = 0.66D$ was set as a criterion for the onset of slugging [1], and defined $\alpha_{s,slugs} = 0.22$ as a maximum solid volume fraction for slug detection. The calculation leading to the value of $\alpha_{s,slugs}$ is detailed in Eq. (7), where V_{slice} and h_{slice} account for the volume and the height of the considered slice, respectively.

$$\alpha_{s,slug} = \frac{\alpha_s(V_{slice} - h_{slice}\pi d_B^2/4) + 0.3h_{slice}\pi d_B^2/4}{V_{slice}} = 0.22 \quad (7)$$

Several peaks under the threshold value highlight the presence of slugs after 50 cm bed height and are in good agreement with experimental results.

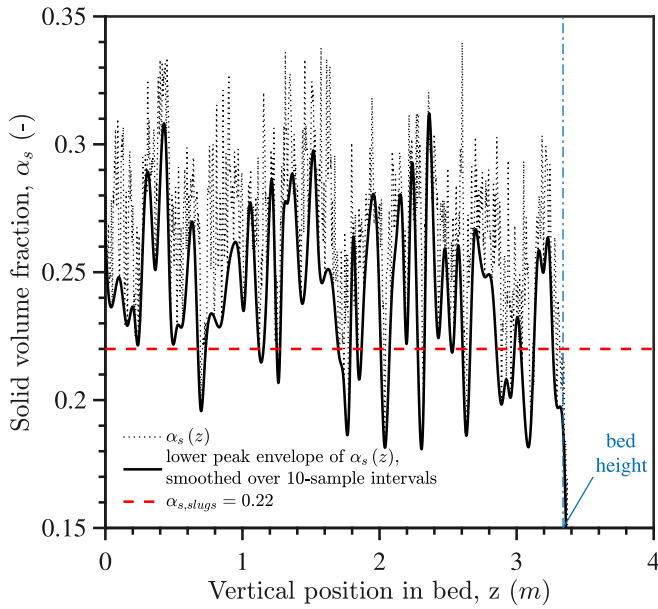


Fig. 14. Instantaneous profile of the spatially averaged solid fraction along the vertical axis z , at $t = 71.9$ s.

Fig. 15 displays the solid volume fraction instantaneous field. Three different views of 70 cm length are represented at different bed levels. The incipient unstructured bubbling at the bottom of the tube (①) is progressively coalescing along the tube, being replaced by local larger dilute structures (②), occupying almost the entire tube diameter and therefore related to slugging. Finally ③, higher up the bed, the dilute structures become longer. Although slugging is clearly predicted, it is yet impossible to distinguish wall and axi-symmetric slugs by the simulation.

4.2.4. Spatio-temporal map of the spatially averaged solid volume fraction, $\alpha_s(z, t)$

Due to the slugging periodicity, the temporal evolution of the solid fraction in a cylindrical slice was studied. Fig. 16 represents the dependence of the aforementioned spatially averaged solid fraction $\alpha_s(z, t)$, on both vertical position and time.

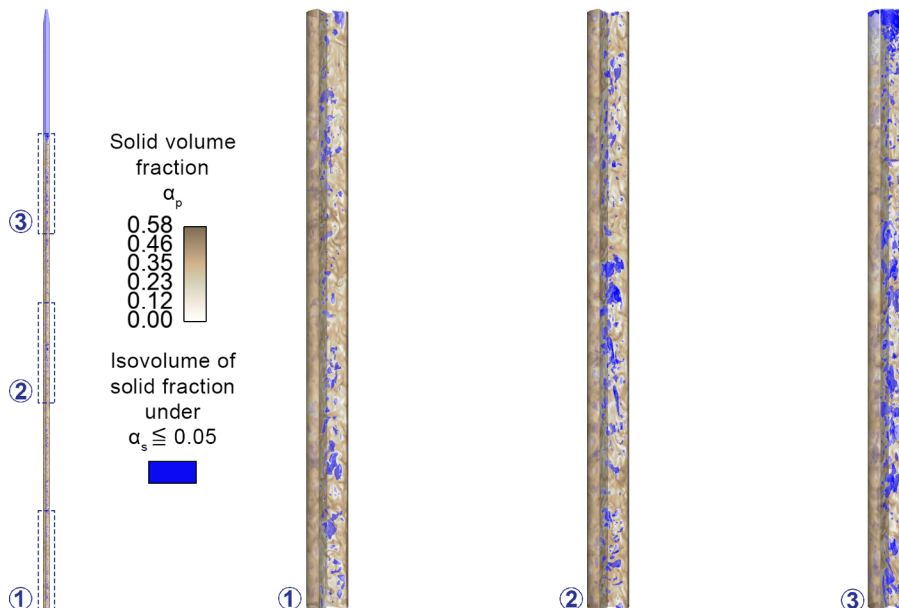


Fig. 15. Instantaneous field of the solid volume fraction at $t = 71.9$ s.

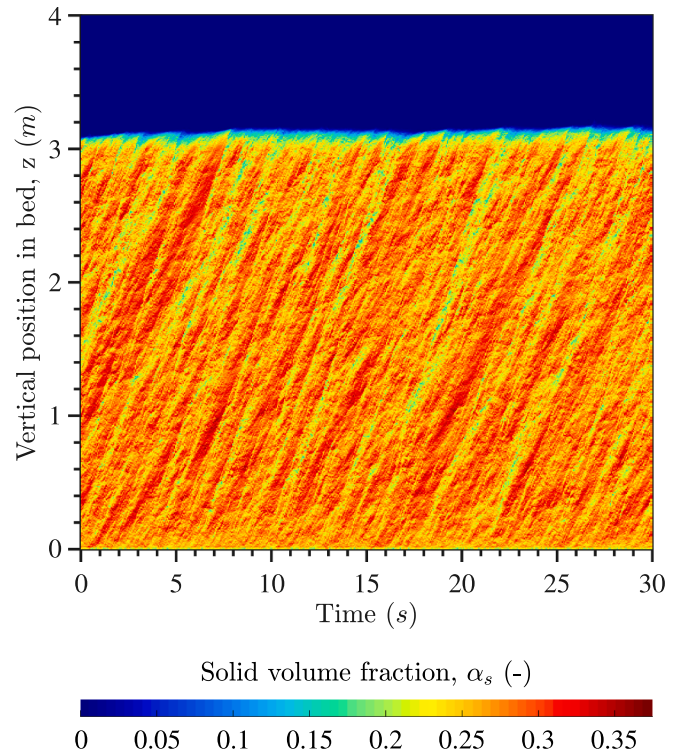


Fig. 16. Instantaneous map of the spatially averaged solid fraction along the vertical axis function of time with t_0 offsets to 30 s of physical time.

A clear fringe pattern evolving periodically along the bed is visible. Considering slugs as a progressive wave propagation along the bed, their vertical velocity was measured graphically with a value of 0.4 m s^{-1} , in good agreement with experimental results for axi-symmetric slugging. In addition, the fringe pattern only appears after a first random region of 0.3 to 0.5 m at the bottom of the bed corresponding to the experimental height for the onset of slugging.

4.2.5. Temporal Fast Fourier Transform of the spatially averaged solid volume fraction at different heights, $\text{FFT}[\alpha_s(t)](z)$

Since slugs can be considered as a periodic wave propagation in the

solid fraction value along the vertical axis z , the frequency analysis of the spatially averaged solid fraction value was performed at different levels in the bed by computing its Fast Fourier Transform (FFT). Fig. 17 highlights these FFT results at three different levels:

- At the bed bottom (0.1 m), the signal is very random with no distinctive frequency, due to the freely bubbling bed behavior and a wide span of bubble sizes and velocities due to bubble coalescence.
- At 1.0 m height, the amplitude of frequencies below 1.8 Hz is higher than lower in the bed, with a similar superimposed random signal as before: bubbles have coalesced but smaller bubbles continue to coincide with larger ones.
- At 3.0 m height, the high amplitude frequencies zone is now under 1 Hz, with stronger peaks, however with a background signal of higher frequencies due to the presence of small bubbles in between slugs.

After the onset on slugging, a higher amplitude zone emerges due to slugs crossing the studied bed level. Bubbles however remain to form a background signal. In line with the experimental results the frequency tends to decrease between 1 m and 3 m height. Furthermore, the temporal and spatial 2D Fast Fourier Transform of the spatially averaged solid fraction was performed leading to similar results as aforementioned. In addition, considering slugging as a progressive wave, their vertical velocity was computed multiplying their frequency by their wave number leading once again to a velocity close to 0.4 m s^{-1} , in good agreement with experimental results for axi-symmetric slugging.

4.2.6. Final assessment of the NEPTUNE_CFD simulation

NEPTUNE_CFD was found to be able to reproduce accurately the bed expansion (pressure drop along the bed and thus the bed height). In addition, large diluted structures related to slugging were successfully predicted, and in good agreement with experimental results concerning their onset height within the bed. Their rise velocity and frequency was found to be of the same order of magnitude as experimental results for axi-symmetric slugs. No wall slugging, with a higher occurrence frequency and higher rise velocity, was distinguishable. The discrepancy

Table 3

Comparison of experimental and simulation results, at $U = 25 \times U_{mf}$.

		Experimental results	Simulation results
Average solid fraction		0.33	0.29
$\delta(\Delta P)/\Delta P$		0.065	0.06
Onset height	wall slugging	0.9 m	>1 m
	axi-symmetric slugging	1.5 m	Between 1 and 3 m
Frequency	wall slugging	1 Hz	No distinction possible, but < 1 Hz
	axi-symmetric slugging	0.5 Hz	
Rise velocity	wall slugging	0.63 m s^{-1}	Not predicted
	axi-symmetric slugging	0.4 m s^{-1}	0.4 m s^{-1}

on $\delta(\Delta P)/\Delta P$ (0.06 against 0.065) is also directly linked to the slug shape. Bigger slugs, as found during experiments, would induce larger pressure drop fluctuations when bursting at the top of the bed. The differences and agreements between experiments and simulation results are summarized in Table 3.

Although experimental and simulation results are in fair agreement, additional improvements are required and in order to enhance the slug description in numerical simulation, several numerical parameters were studied. Fede et al. [45], Goldschmidt et al. [50] have shown that a decrease of particle-particle coefficient e_c trends to increase the formation of bubbles and the suspension heterogeneity. In the present study, a decrease of e_c from 0.9 to 0.7 allowed to keep the same slug velocity and frequency, but did not significantly improve the slugs characteristics, and trends to decrease slightly the total bed height.

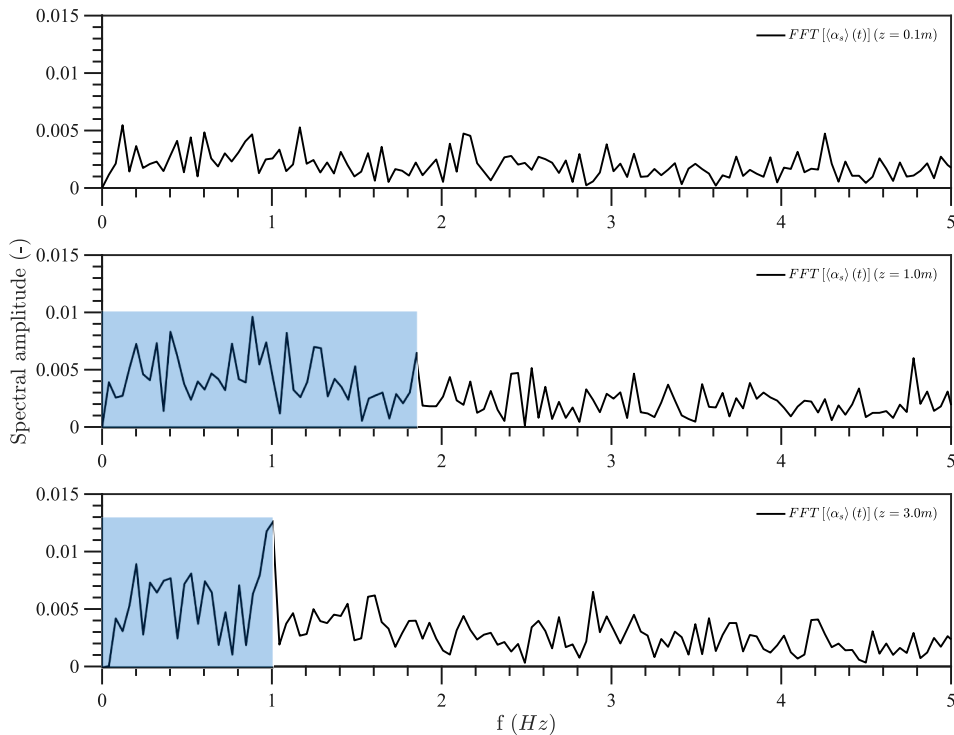


Fig. 17. FFT of the spatially averaged solid fraction $\alpha_s(z, t)$ at three different heights ($z = 0.1 \text{ m}$, $z = 1 \text{ m}$ and $z = 3 \text{ m}$).

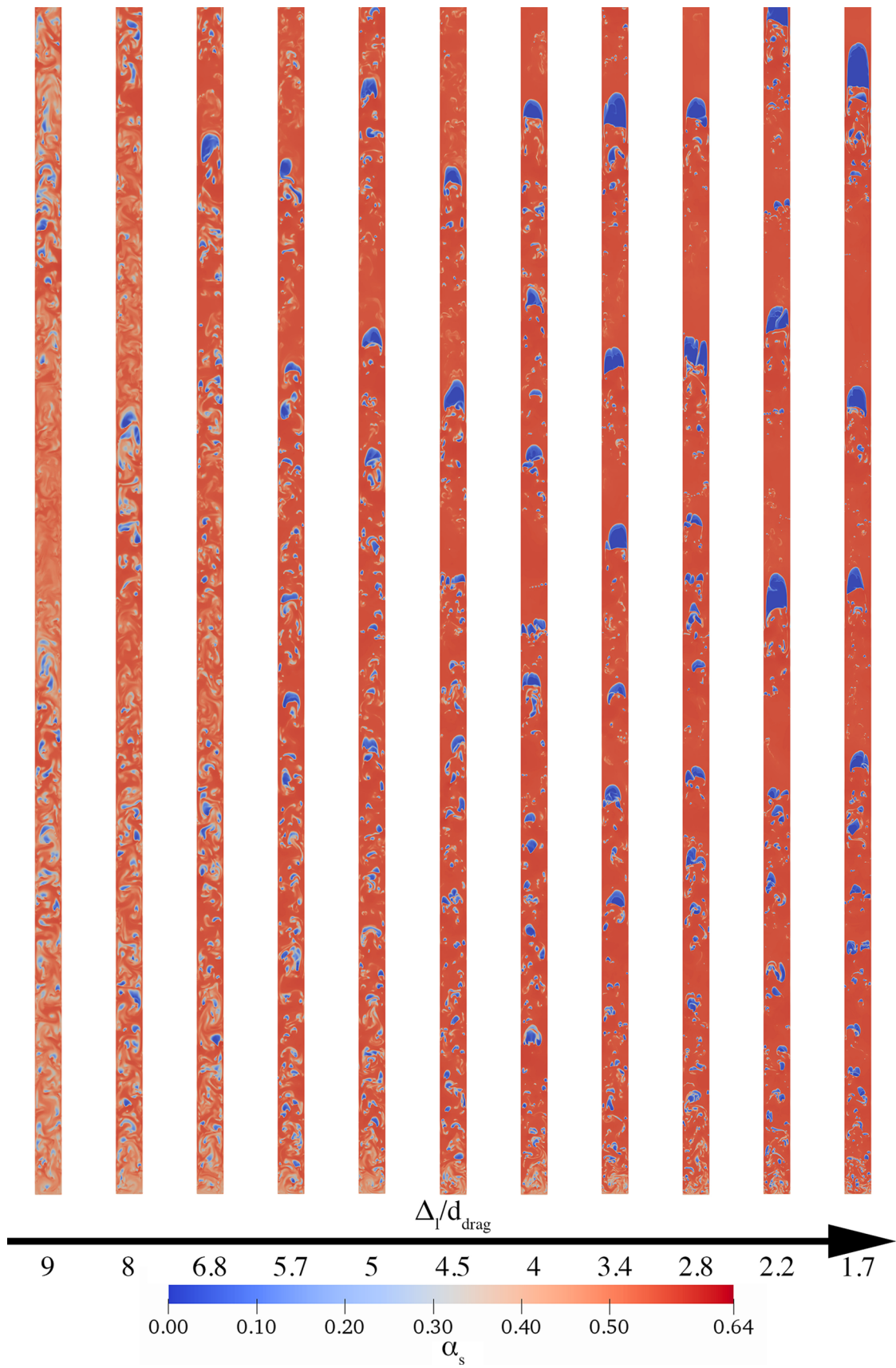


Fig. 18. Study on the impact of the mesh refinement onto slugs description: 2D simulations of a 2 m height geometry, instantaneous field of the solid fraction at the same physical time for each case.

Then, various authors have shown that the particles-wall boundary conditions may have an effect on bubbles structures, bed height and flow internal behavior [51]. Results depicted in this study have been based on a no-slip boundary condition (corresponding to maximum of friction) and elastic particle-wall bouncing. In contrast, the other extreme boundary condition, the free-slip wall boundary conditions (pure elastic frictionless rebounds of spherical particles on a flat wall) has been tested, resulting in a strong diminution of bed height as observed by Fede et al. [45], and without any improvement on slug description.

A comprehensive study was carried out on extremely refined meshes, with cells size from 9 to $1.7 \times d_{drag}$. Since 3D simulations with such a fine mesh cell size are currently impossible to be achieved for in an industrial geometry, these tests were performed in 2D over a 2 m height high fluidized bed of 0.03 m I.D., with multiple cartesian grids. The 3D simulation previously performed corresponds to a cell size of about $14 \times d_{drag}$. Within the studied cell size range, the bed height remained constant but the local flow structure of the particle suspension was substantially modified, according to Fig. 18. Only the bottom 1.3 m of the beds has been represented for clarity reasons. From a cell size of 9 up to $5 \times d_{drag}$, the suspension heterogeneity was emphasised, which allowed for the formation of increasingly larger bubbles structures, but without clearly showing the presence of axi-symmetric slugging. For cell size between 5 and $\sim 2 \times d_{drag}$ however, the suspension heterogeneity kept increasing, showing the formation of slugs with size and shape corresponding to the experimental observations. These extremely refined meshes enabled to capture mesostructures responsible for slug formation. Finally, the transposition of this mesh cell size to the 3D, 4 m high, experimentally studied geometry, would require a $\sim 4,300,000,000$ cell mesh. It is noteworthy that more than just increasing the cell number, the cell size reduction would also imply a time-step duration reduction in order to respect equations resolution stability criteria.

5. Conclusions

Experimental results and simulations implementing an Eulerian n-fluid approach were compared in order to better understand the flow behavior of Geldart group A particles in small I.D. tube within the frame of an Upflow Bubbling Fluidized Bed. Experiments have indicated that the onset height for wall slugs is around 1 m, which is then followed for bed height exceeding 1.5 m by axi-symmetric slugs. The slugging frequency was found to be independent of the gas velocity. Due to both the low velocity and length of axi-symmetric slugs, it is of paramount importance to be able to predict, and thus avoid their formation. Indeed, the presence of axi-symmetric slug has a strong impact on the suspension heat transfer coefficient, in particular within the frame of the solar receiver particle-in-tube concept. 3D simulations were performed using ultra fine mesh of more than 15,000,000 cells. Because of characteristic time of slugging phenomenon, classical post-treatments based time averaged physical quantities have been replaced in favor of new post-treatments necessitating less calculation time to converge. Simulation results were found to be in good agreement with experiments concerning the bed average solid volume fraction and successfully reflect the formation of large bubbles structures, hence highlighting the capability of the NEPTUNE_CFD code to simulate such particles flow.

The onset height of slugging was in fairly good agreement with experimental results but simulation was unable to distinct wall slugging from axi-symmetric slugging. In addition, the slug description in numerical simulation results is not as obvious as with experimental results.

Preliminary simulations, carried out with NEPTUNE_CFD in 2D, highlighted the effect of a strong mesh refinement (beyond the minimum cells size for a converged bed height) over slugs prediction. Slugs with size and shape corresponding to experimental observations were predicted for mesh cell size around $2 \times d_{drag}$ for the studied powder. However, this cells size cannot be suitable for industrial geometries and

thus the development of subgrid models is essential for an accurate representation of slugging regimes of Geldart group A particles.

Finally, Kong et al. [1] tentatively predicted a delay of slugging to deeper bed heights when operating at higher temperatures. Experiments and simulations at higher temperatures up to 475 °C are in the process of being examined.

Acknowledgments

This work was supported by the European Union's Horizon 2020 research and innovation program under Grant Agreement 727762, project Next-CSP. Additional funding was obtained from Beijing Advanced Innovation Center for Soft Matter Science and Engineering of the Beijing University of Chemical Technology. This work was granted access to the HPC resources of CALMIP under the allocation P1132 and of CINES under the allocation gct6938 made by GENCI.

References

- [1] W. Kong, T. Tan, J. Baeyens, G. Flamant, H. Zhang, Bubbling and slugging of Geldart Group A powders in small diameter columns, *Ind. Eng. Chem. Res.* 56 (2017) 4136–4144.
- [2] J. Baeyens, D. Geldart, An investigation into slugging fluidized beds, *Chem. Eng. Sci.* 29 (1974) 255–265.
- [3] D. Geldart, *Gas Fluidization Technology*, John Wiley & Sons Ltd., Chichester, U.K., 1986.
- [4] J. Baeyens, D. Geldart, S.Y. Wu, Elutriation of fines from gas fluidized beds of Geldart A-type powders ' effect of adding superfines, *Powder Technol.* 71 (1992) 71–80.
- [5] D. Kunii, O. Levenspiel, *Fluidization Engineering*, second ed., Butterworth-Heinemann, Boston, 1991.
- [6] W. Kong, B. Wang, J. Baeyens, S. Li, H. Ke, T. Tan, Solids mixing in a shallow cross-flow bubbling fluidized bed, *Chem. Eng. Sci.* (2018).
- [7] Q. Kang, J. Baeyens, H. Zhang, Energy analysis of a particle suspension solar combined cycle power plant, *Energy Convers. Manage.* 613 (2018) 292–303.
- [8] H. Zhang, W. Kong, T. Tan, F. Gilles, J. Baeyens, Experiments support an improved model for particle transport in fluidized beds, *Scientific Rep.* 7 (2017) 10178.
- [9] H. Zhang, H. Benoit, I. Perez-Lopez, G. Flamant, T. Tan, J. Baeyens, High-efficiency solar power towers using particle suspensions as heat carrier and thermal energy storage, *Renew. Energy* 111 (2017) 438–446.
- [10] H.L. Zhang, T. Gowing, J. Degrève, T. Leadbeater, J. Baeyens, The use of particle heat carriers in the Stirling engine concept, *Energy Technol.* (2016).
- [11] H. Zhang, H. Benoit, D. Gauthier, J. Degrève, J. Baeyens, I.P. López, M. Hemati, G. Flamant, Particle circulation loops in solar energy capture and storage: gas-solid flow and heat transfer considerations, *Appl. Energy* 161 (2016) 206–224.
- [12] J. Baeyens, S.Y. Wu, Bed expansion and the visible bubble flow rate in gas fluidized beds, *Adv. Powder Technol.* 3 (1992) 163–189.
- [13] J. Baeyens, D. Geldart, Modelling approach to the effect of equipment scale on fluidized bed heat transfer data, *J. Powder Bulk Solids Technol.* 4 (1980) 1–9.
- [14] J.M. Valverde, M.A. Quintanilla, A. Castellanos, D. Lepek, J. Quevedo, R.N. Dave, R. Pfeffer, Fluidization of fine and ultrafine particles using nitrogen and neon as fluidizing gases, *AIChE J.* 54 (2008) 86–103.
- [15] M. Ye, J. Wang, M.A. van der Hoef, H. Kuipers, Two-fluid modeling of Geldart A particles in gas-fluidized beds, *Particuology* 6 (2008) 540–548.
- [16] H.L. Zhang, J. Degrève, R. Dewil, J. Baeyens, Operation diagram of circulating fluidized beds (CFBs), *Proc. Eng.* 102 (2015) 1092–1103.
- [17] F. Pitie, C.Y. Zhao, J. Baeyens, J. Degrève, H.L. Zhang, Circulating fluidized bed heat recovery/storage and its potential to use coated phase-change-material (PCM) particles, *Appl. Energy* 109 (2013).
- [18] C.W. Chan, J.P.K. Seville, D.J. Parker, J. Baeyens, Particle velocities and their residence time distribution in the riser of a CFB, *Powder Technol.* 203 (2010) 187–197.
- [19] H. Zhang, W. Kong, T. Tan, J. Baeyens, High-efficiency concentrated solar power plants need appropriate materials for high-temperature heat capture, conveying and storage, *Energy* 139 (2017) 52–64.
- [20] G. Flamant, D. Gauthier, H. Benoit, J.L. Sans, R. Garcia, B. Boissière, R. Ansart, M. Hemati, Dense suspension of solid particles as a new heat transfer fluid for concentrated solar thermal plants: on-sun proof of concept, *Chem. Eng. Sci.* 102 (2013) 567–576.
- [21] I. Perez-Lopez, H. Benoit, D. Gauthier, J.-L. Sans, E. Guillot, G. Mazza, G. Flamant, On-sun operation of a 150kWth pilot solar receiver using dense particle suspension as heat transfer fluid, *Sol. Energy* 137 (2016) 463–476.
- [22] Torresol Energy, Gemasolar, 2015.
- [23] R. Ansart, P. García-Triñanes, B. Boissière, H. Benoit, J.P.K. Seville, O. Simonin, Dense gas-particle suspension upward flow used as heat transfer fluid in solar receiver: PEPT experiments and 3D numerical simulations, *Powder Technol.* 307 (2017) 25–36.
- [24] D. Geldart, J. Baeyens, The design of distributors for gas-fluidized beds, *Powder Technol.* 42 (1985) 67–78.
- [25] I. Cavarretta, C. O'Sullivan, M.R. Coop, Applying 2D shape analysis techniques to

- granular materials with 3D particle geometries, in: AIP Conference Proceedings, vol. 1145, pp. 833–836.
- [26] G.-C. Cho, J. Dodds, J.C. Santamarina, Particle shape effects on packing density, stiffness, and strength: natural and crushed sands, *J. Geotech. Geoenviron. Eng.* 132 (2006) 591–602.
- [27] M. Leva, M. Weintraub, M. Grummer, M. Pollchik, H.H. Storch, *Fluid Flow Through Packed and Fluidized Systems*, (Bulletin. Bureau of Mines), U.S. Government Printing Office, 1951.
- [28] J. Xie, W. Zhong, B. Jin, Y. Shao, Y. Huang, Eulerian-Lagrangian method for three-dimensional simulation of fluidized bed coal gasification, *Adv. Powder Technol.* 24 (2013) 382–392.
- [29] Z. Hamidouche, E. Masi, P. Fede, R. Ansart, H. Neau, M. Hemati, O. Simonin, Numerical Simulation of Multiphase Reactive Flows, in: *Advances in Chemical Engineering*, vol. 52, 2018, pp. 51–124.
- [30] H. Benoit, R. Ansart, H. Neau, P. Garcia Triñanes, G. Flamant, O. Simonin, Three-dimensional numerical simulation of upflow bubbling fluidized bed in opaque tube under high flux solar heating, *AIChE J.* 64 (2018) 3857–3867.
- [31] F. Fotovat, R. Ansart, M. Hemati, O. Simonin, J. Chaouki, Sand-assisted fluidization of large cylindrical and spherical biomass particles: experiments and simulation, *Chem. Eng. Sci.* 126 (2015) 543–559.
- [32] P. Fede, O. Simonin, I. Ghouila, 3D Numerical Simulation of Polydisperse Pressurized Gas-Solid Fluidized Bed, in: *ASME-JSME-KSME 2011 Joint Fluids Engineering Conference*, 44403, pp. 3199–3210.
- [33] N. Méchitoua, M. Boucker, J. Laviéville, S. Pigny, G. Serre, An unstructured finite volume solver for two phase water/vapour flows based on an elliptic oriented fractional step method, in: *NURETH 10*, Seoul, South Korea.
- [34] S. Morioka, T. Nakajima, Modeling of gas and solid particles two-phase flow and application to fluidized bed, *J. Theor. Appl. Mech.* 6 (1987) 77–78.
- [35] A. Boelle, G. Balzer, O. Simonin, Second-order prediction of the particle-phase stress tensor of inelastic spheres in simple shear dense suspensions, *ASME-Publications-Fed* 228 (1995) 9–18.
- [36] A. Srivastava, S. Sundaresan, Analysis of a frictional-kinetic model for gas-particle flow, *Powder Technol.* 129 (2003) 72–85.
- [37] C. Wen, Y. Yu, *Mechanics of fluidization*, *Chem. Eng. Symp. Ser.* 62 (1965) 100–111.
- [38] S. Ergun, Fluid flow through packed columns, *Chem. Eng. Prog.* 48 (1952) 89–94.
- [39] A. Gobin, H. Neau, O. Simonin, J.-R. Llinas, V. Reiling, J.-L. Sélo, Fluid dynamic numerical simulation of a gas phase polymerization reactor, *Int. J. Numer. Meth. Fluids* 43 (2003) 1199–1220.
- [40] O. Simonin, S. Chevrier, F. Audard, P. Fede, Drag force modelling in dilute to dense particle-laden flows with mono-disperse or binary mixture of solid particles, in: *9th International Conference on Multiphase Flow*.
- [41] F. Sabatier, A. Renaud, W. Kong, H. Zhang, J. Baeyens, G. Flamant, O. Simonin, Bubbling of Geldart Group A Powders in Small Diameter Columns: Experiments and 3D Numerical Simulations focussing on the particle size distribution and non sphericity, in: *World Congress on Particle Technology VIII*, Orlando, FL.
- [42] G.H. Bagheri, C. Bonadonna, On the drag of freely falling non-spherical particles, *Powder Technol.* 301 (2016) 526–544.
- [43] K. Agrawal, P.N. Loezos, M. Syamlal, S. Sundaresan, The role of meso-scale structures in rapid gas-solid flows, *J. Fluid Mech.* 445 (2001) 151–185.
- [44] J.-F. Parmentier, O. Simonin, O. Delsart, A functional subgrid drift velocity model for filtered drag prediction in dense fluidized bed, *AIChE J.* 58 (2012) 1084–1098.
- [45] P. Fede, O. Simonin, A. Ingram, 3D numerical simulation of a lab-scale pressurized dense fluidized bed focussing on the effect of the particle-particle restitution coefficient and particle-wall boundary conditions, *Chem. Eng. Sci.* 142 (2016) 215–235.
- [46] H. Neau, J. Laviéville, O. Simonin, NEPTUNE_CFD High Parallel Computing Performances for Particle-Laden Reactive Flows, in: *7th International Conference on Multiphase Flow*, Tampa, FL.
- [47] J. Werther, Hydrodynamics and mass transfer between the bubble and emulsion phases in fluidized beds of sand and cracking catalyst, *Proc. 4th Int Conf. On Fluidization* (1983) 93–101.
- [48] R. Yamazaki, M. Nakajima, N. Ueda, G. Jimbo, *Fluidization'85 Science and Technology* (1985).
- [49] A.W. Weimer, G.J. Quarderer, On dense phase voidage and bubble size in high pressure fluidized beds of fine powders, *AIChE J.* 31 (1985) 1019–1028.
- [50] M.J. Goldschmidt, J.A. Kuipers, W.P. Van Swaaij, Hydrodynamic modelling of dense gas-fluidised beds using the kinetic theory of granular flow: effect of coefficient of restitution on bed dynamics, *Chem. Eng. Sci.* 56 (2001) 571–578.
- [51] S. Benyahia, M. Syamlal, T.J. O'Brien, Evaluation of boundary conditions used to model dilute, turbulent gas/solids flows in a pipe, *Powder Technol.* 156 (2005) 62–72.